

RC-Oscillator-Based Battery-Less Wireless Sensing System Using RF Resonant Electromagnetic Coupling

Zixuan LI^{†a)}, Nonmember, Sangyeop LEE[†], Noboru ISHIHARA[†], and Hiroyuki ITO[†], Members

SUMMARY A wireless sensor terminal module of 5cc size (2.5 cm × 2.5 cm × 0.8 cm) that does not require a battery is proposed by integrating three kinds of circuit technologies. (i) a low-power sensor interface: an FM modulation type CMOS sensor interface circuit that can operate with a typical power consumption of 24.5 μW was fabricated by the 0.7-μm CMOS process technology. (ii) power supply to the sensor interface circuit: a wireless power transmission characteristic to a small-sized PCB spiral coil antenna was clarified and applied to the module. (iii) wireless sensing from the module: backscatter communication technology that modulates the signal from the base terminal equipment with sensor information and reflects it, which is used for the low-power sensing operation. The module fabricated includes a rectifier circuit with the PCB spiral coil antenna that receives wireless power transmitted from base terminal equipment by electromagnetic resonance coupling and converts it into DC power and a sensor interface circuit that operates using the power. The interface circuit modulates the received signal with the sensor information and reflects it back to the base terminal. The module could achieve 100 mm communication distance when 0.4 mW power is feeding to the sensor terminal.

key words: battery-less, wireless sensing, wireless power transmission, sensor interface circuit, CMOS integrated circuit, FM modulation, oscillator

1. Introduction

IoT (Internet of Things) technology [1], [2] is spreading in various fields and areas, and the sensor network that supports it requires an enormous number of sensor terminals. Thus, cost reduction, low power consumption, and miniaturization of terminals are required. In particular, low power consumption is expected to have an effect on reducing maintenance costs since battery life can be prolonged and battery-less operation in which battery replacement work is not required can be expected. In logistics systems, the transport of luggage is controlled by ID tags [3]. However, for cardboard or Styrofoam boxes packed with fresh food, sensors that can monitor temperature and humidity inside enclosed spaces for quality control purposes are expected [4].

The monitoring of the closed space is anticipated to be applied not only to the logistics systems but also to the sensing in the living body such as the oral cavity in the medical field, and the monitoring in the building structure [5], [6].

For these reasons, research and development of a wireless low-power consumption sensor terminal module are be-

ing promoted. For example, a battery-less operation is realized by combining Bluetooth with rectenna and operating intermittently [7], [8]. And there is a wireless communication system called RoLa that can transmit a small amount of information but cover a wide communication area with low power has been proposed [9], [10]. However, in these systems, the communication distance can be ensured, but the antenna size limits the miniaturization because the UHF band RF signal is used.

To realize a small battery-less wireless sensing module, we focused on integrating three kinds of circuit technologies. (i) a low-power sensor interface: an FM modulation type CMOS sensor interface circuit that can operate with low power supply. (ii) a power supply for the sensor interface circuit: a wireless power transmission characteristic to a small-sized PCB coil antenna were clarified and applied to the module. (iii) wireless sensing from the module: backscatter communication technology that modulates the signal from the base terminal equipment with sensor information and reflects it is used for the low power sensing operation.

By combining these technologies, we designed and made a prototype of a small wireless sensor terminal module that does not require a battery. The module consists of a PCB spiral coil antenna, a rectifier circuit, and a sensor interface circuit. The sensor interface circuit was integrated with a low-cost 0.7-μm CMOS technology, achieving 24.5 μW low-power operation. The rectifier circuit uses full bridge rectifier IC: NMLU1210. The module size is 5cc (2.5 cm × 2.5 cm × 0.8 cm). When the power signal of 5 MHz was radiated to the sensor module, the sensing operation without a battery was successfully realized. The maximum communication distance was about 100 mm.

In this paper, the design and the configuration methodology of the battery-less wireless sensor terminal module are discussed. Section 2 introduces the design concept of the proposed module that integrates three kinds of circuit technologies. Sections 3 to 5 discuss detailed circuit techniques for each technology. Section 6 describes the evaluation results of the module fabricated to confirm the effectiveness of the circuit technology, and Sect. 7 concludes.

2. Design Concept of Proposed Module

2.1 Wireless Sensing

Figure 1(a) shows the conventional wireless sensing sys-

Manuscript received May 21, 2023.

Manuscript revised September 11, 2023.

Manuscript publicized November 24, 2023.

[†]The authors are with Nano Sensing Unit, Institute of Innovative Research, Tokyo Institute of Technology, Yokohama-shi, 226-8503 Japan.

a) E-mail: li.z.aq@m.titech.ac.jp

DOI: 10.1587/transfun.2023GCP0002

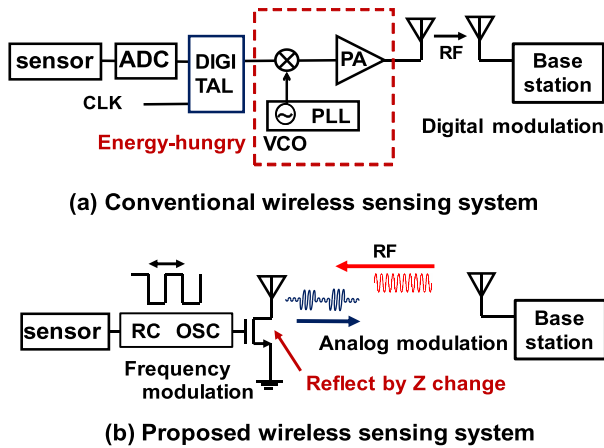


Fig. 1 Wireless sensing system.

tem [11]–[15]. In this system, the sensor information is converted into digital data by an analog-to-digital conversion circuit, and the circuit configuration transmits a high-frequency digitally modulated signal to the base station. The wireless transmission circuit consists of a phase-locked loop circuit and a power amplifier and requires power of at least 1 mW or more.

First of all, in order to achieve battery-less operation, it is essential that the sensor interface circuit and the wireless transmitter circuit operate at low power. To meet this target, we employed an analog domain wireless sensing system as shown in Fig. 1(b). RC relaxation oscillator (OSC) was used as a sensor interface to be operated with lower power. By using this, the resistance or capacitance type sensor can be connected directly, and sensor value change can be observed as frequency variation, in other words, frequency modulation (FM) signal. To transmit the sensor information to the base station, we employed backscatter technology that uses signal reflection to transmit the information to the base station that was used in the RFID system [16], [17]. The RF signal from the base station is reflected back depending on the mismatch condition between the antenna and a MOS-FET output. As the output impedance is switched with the RC-OSC output signal, the received signal is modulated and reflected back. In this configuration, energy-hungry transmit circuitry is not required and the reflection operation consumes no power, significantly lower power operation is possible.

2.2 Wireless Power Supply

As shown in Fig. 2, there are two methods of wireless power supply, one that uses radio wave energy and the other that uses electromagnetic coupling. The former requires consideration of the trade-off between antenna size and RF signal frequency. Assuming a 1 GHz signal, from the wavelength the antenna size should be 15 cm. The latter, on the other hand, uses a coil instead of an antenna which is powered by a low-frequency signal such as less than 10 MHz. Although the communication distance is as short as a few centimeters,

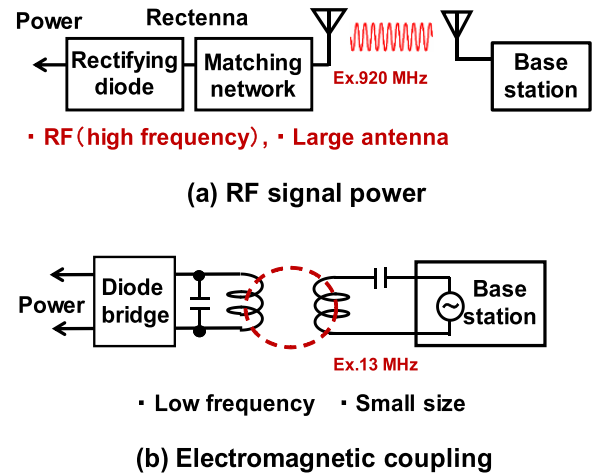


Fig. 2 Wireless power supply.

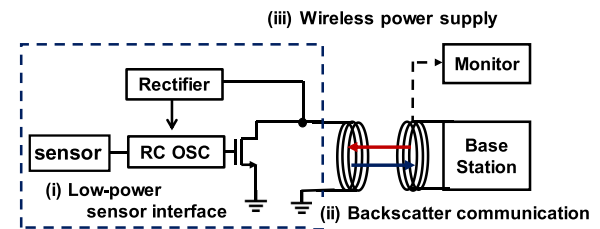


Fig. 3 Proposed sensing system.

Table 1 Design target specifications.

Item	Functions/Values
Target Application	Sensing in invisible areas (delivery boxes, structural buildings, and living organisms)
Module Operation	Wireless & Battery-less
Communication distance	More than 50 mm
Sensing circuit	RC oscillator
Sensing frequency	100 kHz to 1MHz (FM modulated)
Connectable sensors	Capacitor and resistance type
Wireless sensing	Signal backscattering
Power consumption	Less than 1mW
Wireless power supply	Electromagnetic coupling
Power supply frequency	~ 10 MHz
Module size	Less than 5 cc

it has the advantage of allowing the coil to be miniaturized.

2.3 Proposed Battery-Less, Wireless Sensing System

Based on the above basic studies, the proposed sensing system was configured as shown in Fig. 3. Assuming application to battery-less monitoring in invisible closed spaces such as delivery boxes, structural buildings, and living organisms, (i) RC-OSC circuit is used as the sensor interface circuit, (ii) sensor information is transmitted by backscatter technology, (iii) electromagnetic field coupling technology with coils are used for wireless power supply.

The design target specifications are summarized in Table 1. Each detailed technology will be described in detail

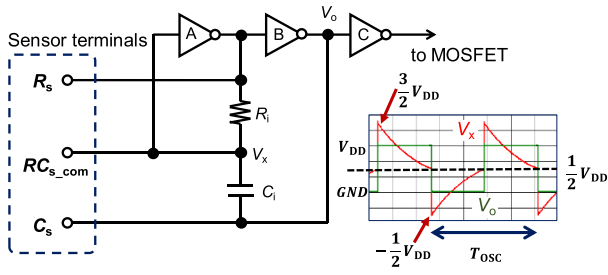


Fig. 4 Inverter base RC relaxation oscillator.

in the following sections.

3. Low-Power Sensor Interface Circuit

3.1 RC Relaxation Oscillator

An inverter-based RC relaxation oscillator circuit shown in Fig. 4 was adopted as the sensor interface circuit [18]. Its operation is as follows.

When the node voltage V_x is 0 V in the initial state and the output of the inverter A is at high level, the capacitor C_i starts to be charged via the resistor R_i , and V_x increases due to charge accumulation. When V_x exceeds the threshold voltage ($V_{DD}/2$) of inverter A, the output of inverter A changes to the low level, and the output of inverter B changes to the high level. At this time, while the voltage of V_x is held, it jumps up by the power supply voltage V_{DD} , and then, discharge from C_i to the output of the inverter A is started via R_i . When V_x falls below the threshold voltage ($V_{DD}/2$) of inverter A, it shifts to the charging mode again. This action is automatically repeated. The oscillation period T_{OSC} is determined by the time constant of R_i and C_i and can be expressed by the following equation.

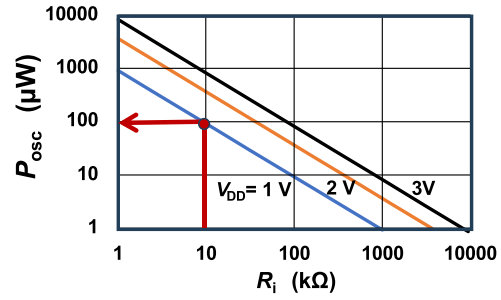
$$T_{OSC} = 2 \ln 3 \cdot R_i \cdot C_i \quad (1)$$

When the change in R_i or C_i due to sensor connection can be detected as a shift in T_{OSC} or in oscillation frequency $f_{osc} = 1/T_{OSC}$.

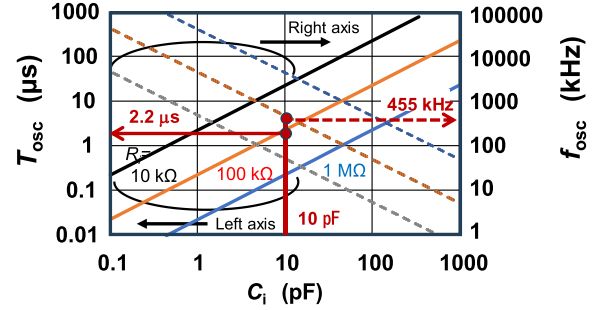
The power consumption P_{OSC} of this circuit can be expressed by the following equation, considering that it is mainly consumed in the charge/discharge operation to C_i .

$$P_{OSC} = \frac{V_{DD}^2}{\ln 3 \cdot R_i} \quad (2)$$

P_{OSC} is determined by the value of R_i and V_{DD} . Figure 5(a) shows the relationship between P_{osc} and R_i obtained from this equation. The three lines show characteristics under the conditions of $V_{DD} = 1$ V, 2 V, and 3 V, respectively. From these characteristics, it is noticeable that the power consumption is less than $100 \mu\text{W}$ when R_i is set more than $10 \text{ k}\Omega$ with $V_{DD} = 1$ V. Figure 5(b) shows the relationship between the oscillation time period T_{OSC} and the oscillation frequency f_{osc} with respect to the capacitance C_i obtained from Eq. (1). For example, when C_i is 10 pF and R_i is $100 \text{ k}\Omega$, T_{OSC} is $2.2 \mu\text{s}$ and f_{osc} is 455 kHz .



(a) Relation between P_{osc} and R_i



(b) Relation between T_{osc} and C_i

Fig. 5 Characteristics of RC relaxation oscillator.

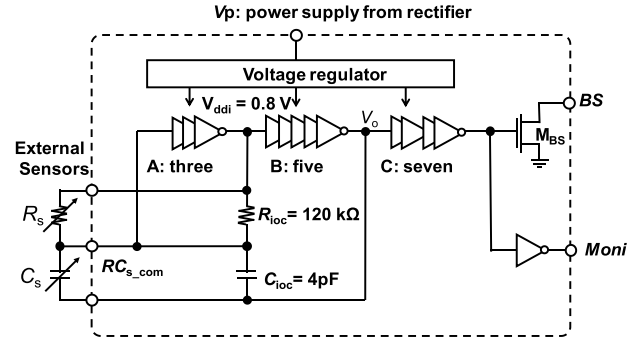


Fig. 6 Circuit for monolithic integration.

3.2 Monolithic Integration

Monolithic integration of the circuit is effective for realizing highly reliable small modules. For this reason, the RC oscillator circuit shown in Fig. 6 was integrated using $0.7\text{-}\mu\text{m}$ CMOS process technology [19]. Advanced integrated circuit technology is not required since the RC oscillator operating speed is dropping to less than 1 MHz . The integrated circuit technology was chosen considering manufacturing cost.

In the integrated circuit, besides the RC oscillation circuit, the voltage regulator and the MOSFET M_{BS} for the backscatter are also integrated. The operation and design of the M_{BS} is described in Sect. 5. The RC oscillator has a multi-stage configuration of inverters to secure gain so that stable operation at 1 V is possible. The number of stages is a combination of 3, 5, and 7 stages so that the inverter

operation of each part does not interfere [20]. The circuit was designed to oscillate above 800 kHz for initial operation with no external sensors connected. A resistance R_{ioc} and a capacitance C_{ioc} were integrated on chip to guarantee initial oscillation operation. The R_{ioc} is set to be large as 120 k Ω and the C_{ioc} is set to be small as 4 pF to support connecting the external resistive or capacitive sensors which are connected in parallel. This is because the adjustable frequency range becomes small with the external sensors when the R_{ioc} is small and the C_{ioc} is large. From the circuit simulation without the external sensors for Fig. 6, T_{OSC} was 1.2 μ s and thus f_{OSC} became about 830 kHz. However, calculating from Eq. (1) substituting 120 k Ω of R_{ioc} to R_i , and 4 pF of C_{ioc} to C_i , T_{OSC} becomes 1.05 μ s and f_{OSC} is about 950 kHz. As a result of examining the reason why T_{OSC} in the circuit simulation result is about 0.15 μ s larger than the calculation result, we found that it is due to the propagation delay time of the multi-stage CMOS inverters. Equivalently converting the delay time as a capacitance C_{pd} results in 0.6 pF. As the value of C_i in Eq. (1), the sum of C_{ioc} and C_{pd} , which is 4.6 pF, is considered in the circuit design.

The voltage regulator is a common configuration and enables a low voltage output of 1 V.

3.3 Fabrication Results of Sensor Interface IC

Figure 7(a) shows a microphotograph of a fabricated chip. Its size is 1.15 mm square. For the evaluation, the bare chip is mounted directly on the PCB board, connected to the board with bonding wires, and covered with resin for protection as shown in Fig. 7(b).

Figure 8(a) shows the dependence of the oscillation frequency on the power supply voltage. It is observable that the oscillation frequency f_{osc} is stabilized when the power supply voltage V_p exceeds 1 V. The f_{osc} was 758 kHz which is smaller than the designed value of the IC chip, 830 kHz. This is because T_{OSC} further increases and f_{OSC} decreases due to the parasitic capacitance C_{bd} at the connection between the IC and the substrate wiring. C_{bd} is estimated to be 0.4 pF, and the capacitance is to be considered as C_i in Eq. (1) is the sum of C_{ioc} , C_{pd} , and C_{bd} , which is 5 pF. In the IC design with the board, it is important to consider the effects of the propagation delay of the CMOS inverters and the parasitic capacitance of the connection with the board wiring. The frequency change was 25 kHz (3% of f_{osc}) when V_p was changed from 1 V to 3 V.

Figure 8(b) shows the results of evaluating the power supply voltage dependence of the output signal amplitude V_a . It can be seen that V_a stabilizes at the voltage regulator's output voltage of 0.8 V. The current consumption of the circuit was 25 μ A, and the power consumption at $V_p = 1$ V became 25 μ W. The power consumption of the oscillator circuit part is about 4 μ W from Eq. (2), and most of the power is consumed by the voltage regulator circuit and output driver circuit for monitoring.

Figure 9 exhibits the results of measuring changes in oscillation frequency due to changes in external resistor R_s

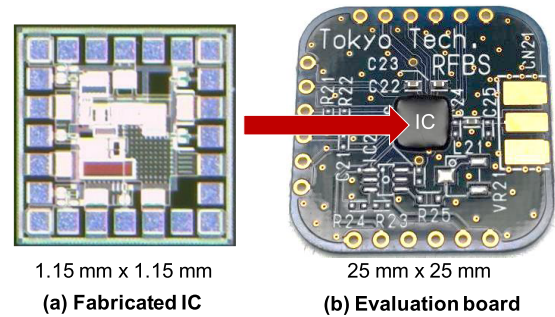
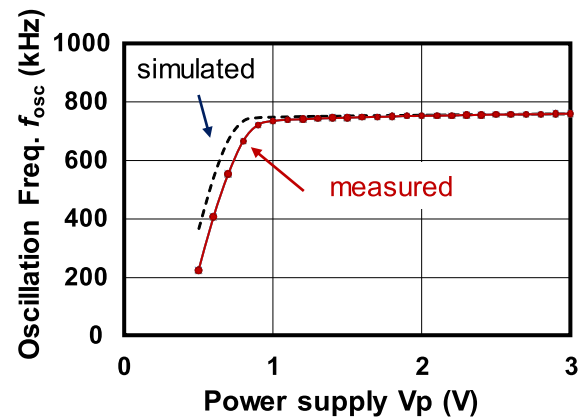
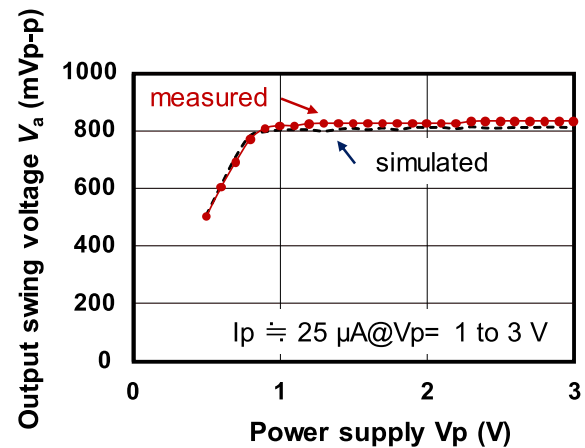


Fig. 7 Microphotograph of fabricated chip and sensor interface evaluation board.



(a) Oscillation Frequency



(b) Output swing voltage

Fig. 8 Characteristics of fabricated chip.

and external capacitor C_s , assuming connection with resistive or capacitive sensor devices. The horizontal axis is the value of the external resistance R_s , and the three characteristics are the characteristics when external capacitances are 10 pF, 33 pF, and 100 pF. The solid lines are the measurement results, and the dashed lines are the calculation results by Eq. (1). In the calculation with Eq. (1), R_i is the total resistance of paralleled R_s and R_{ioc} (120 k Ω). C_i is 5 pF which

is the sum of C_s , C_{ioc} , C_{pd} , and C_{bd} .

By combining 10 pF to 100 pF capacitance C_s and 20 k Ω to 1000 k Ω R_s , 40 kHz to 1000 kHz oscillation output range can be obtained. The circuit worked with the resistance value of R_s above 20 k Ω . If it is lower than 20 k Ω , the input and output of inverter A shown in Fig. 4 are strongly coupled, which suppresses oscillation. In Fig. 9, the deviation from the calculated results in the range of R_s from 20 k Ω to 100 k Ω is due to this coupling.

For temperature measurement, assuming a thermistor as R_s , and assuming that the resistance changes from 20 k Ω to 500 k Ω with temperature changes, the oscillation frequency will change from 1000 kHz to 300 kHz when combined with C_s of 10 pF. Specific application results for temperature measurement are described in Sect. 6.

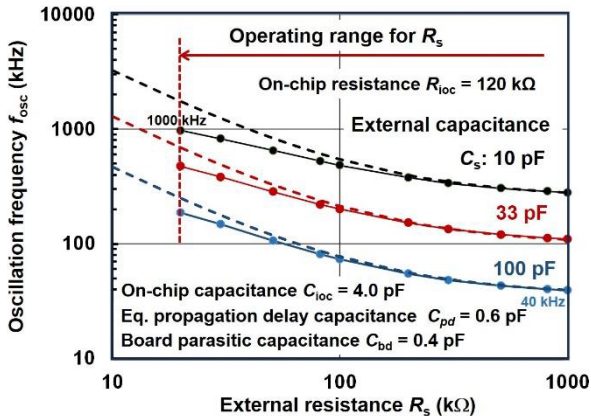


Fig. 9 Dependence on external resistance and capacitance.

4. Wireless Power Supply

4.1 Magnetic Resonance Coupling

We focused on magnetic resonance coupling technology [21], [22] as a wireless supply method for the sensor interface IC. As shown in Table 2, there are four possible configurations for magnetic resonance power transmission, depending on the combination of series and parallel resonance circuits on the power transmitting side and the receiving side [23]–[25]. Additionally, L_1 and L_2 represent the inductance of two coils, r_1 and r_2 are for the parasitic resistance of the coils, and C_1 and C_2 work as the resonance capacitance for two coils, Q_1 and Q_2 are quality factor, ω_r is the resonance angle frequency, M is the mutual inductance.

Firstly, for the purpose of grasping the fundamental characteristics, the frequency responses were analyzed using a T-type equivalent circuit. Figure 10 shows the simulation results of the frequency responses of the series-series magnetic resonance coupling, and the parameters of the circuit are marked in the figure. Realistic resonance parameter values were set and analyzed so that the resonance frequency f_r would be 10 MHz. The coupling coefficient k was set to 0.1. The impedance modifications on both the power transmitting and power receiving sides give rise to a variety of distinctive characteristics. It can be seen that in this serial-serial resonance type, at a resonance frequency of 10 MHz, the maximum transmission gain S_{21} and the matching characteristic S_{11} (minimum reflection) with maximum power supply are obtained at $R_s = R_L = 6.35 \Omega$. This value can be given by the equation of $R_{L,opt}$, which is the optimized resistance to get η_{max} in Table 2.

When R_s and R_L are lower than $R_{L,opt}$, which is 6.35 Ω ,

Table 2 Wireless power transmission with magnetic resonance.

		resonance Secondary coil resonance (Receiving side)	
		Serial LC	Parallel LC
Primary coil resonance (Transmitting side)	Serial LC		
	Parallel LC		
Efficiency η		$\eta = \frac{I_2^2 \cdot R_L}{I_1 \cdot V_1}$ $= \frac{1}{(1 + \frac{r_2}{R_L}) (\frac{1}{k^2 \cdot Q_1 \cdot Q_2} (1 + \frac{R_L}{r_2}) + 1)}$ $Q_1 = \frac{\omega_r \cdot L_1}{r_1} \quad Q_2 = \frac{\omega_r \cdot L_2}{r_2} \quad M = k\sqrt{L_1 \cdot L_2}$	$\eta = \frac{V_2^2 / R_L}{I_1 \cdot V_1}$ $= \frac{1}{1 + \frac{R_L}{Q_2^2 \cdot r_2} + \frac{r_2}{R_L} (1 + \frac{1}{k^2 \cdot Q_1 \cdot Q_2} + \frac{Q_2}{k^2 \cdot Q_1})}$ $Q_1 = \frac{\omega_r \cdot L_1}{r_1} \quad Q_2 = \frac{\omega_r \cdot L_2}{r_2} \quad M = k\sqrt{L_1 \cdot L_2}$
Maximum η_{max}		$\eta_{max} = \frac{1}{\frac{1}{k^2 \cdot Q_1 \cdot Q_2} (1 + \sqrt{1 + k^2 \cdot Q_1 \cdot Q_2})^2}$ $R_{L,opt} = r_2 \sqrt{1 + k^2 \cdot Q_1 \cdot Q_2}$	$\eta_{max} = \frac{1}{1 + \frac{2}{k\sqrt{Q_1 \cdot Q_2}} \sqrt{1 + \frac{k^2}{Q_2} + \frac{1}{Q_2^2}}}$ $R_{L,opt} = Q_2 \cdot r_2 \sqrt{1 + \frac{1}{k^2} (\frac{1}{Q_1 \cdot Q_2} + \frac{Q_2}{Q_1})}$

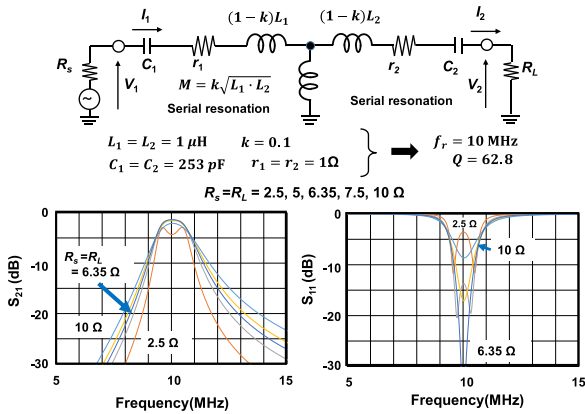


Fig. 10 Serial-serial magnetic resonance coupling.

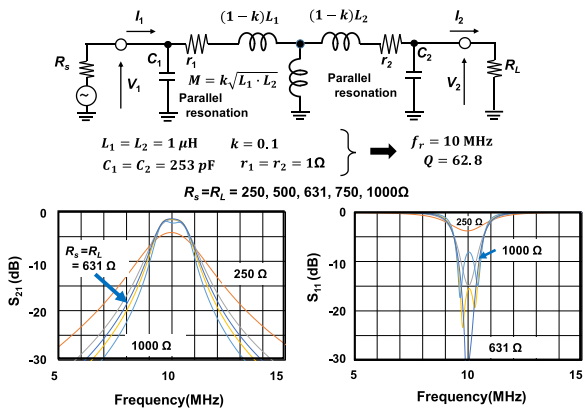


Fig. 11 Parallel-parallel magnetic resonance coupling.

two peaks appear in the frequency characteristics [26]. This is due to the strong resonance coupling. The two frequencies are about $\sqrt{1 \pm k}$ times of the resonance frequency $f_r = \omega_r / (2\pi)$. Furthermore, as the value of the coupling coefficient k increases, the value of $R_{L,opt}$ also increases, and two frequency peaks become prominent.

Figure 11 shows the parallel-parallel resonant type simulation results. In this case, the transmission characteristics are maximized when $R_{L,opt} = R_s = R_L = 631 \Omega$. Compared to the serial-serial resonant type, the values of $R_{L,opt}$ are about 100 times higher. In this case, when R_s and R_L are greater than 631Ω , two peaks appear in the frequency characteristics. This is also due to the strong resonance coupling.

The power transmission efficiency η can be expressed by the equations in Table 2. Figure 12 shows the results of calculating the efficiency η when the value of R_L is changed. A plurality of characteristics manifests when the Q values of resonance are changed for different resonance types. The value of R_L that maximizes the power efficiency η is higher when the resonance circuit on the power receiving side is of parallel type than when it is of series type. In general, the efficiency η can be increased by increasing the kQ product. When the Q value of resonance is 62.8, the maximum efficiency η_{max} is 0.73 for the series resonance type and 0.76 for

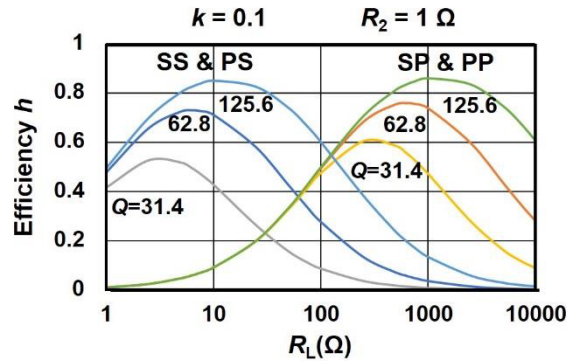


Fig. 12 Wireless power transfer efficiency.

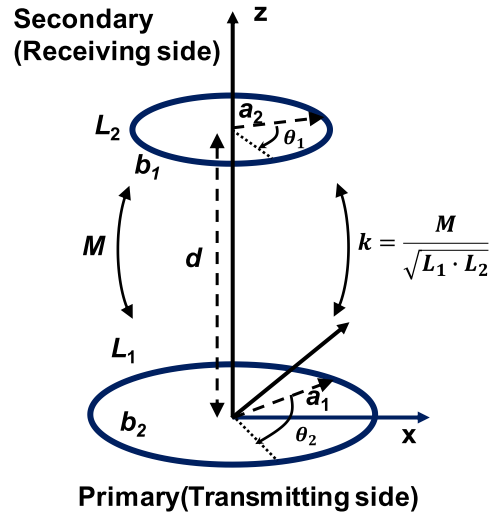


Fig. 13 Simple geometry of magnetic coupling efficiency.

the parallel resonance type, and the R_L values at that condition are 6.35Ω and 631Ω , respectively.

From the above results, it can be concluded that the series type is suitable for a low-resistance load R_L and the parallel type is suitable for a high-resistance load R_L . Since the sensor interface IC has low power consumption with high impedance, a parallel resonance type is selected for the secondary coil on the receiving side, and a series resonance type configuration is selected for the transmitter side assuming low signal source impedance.

4.2 Transmission Range

The value of the coupling coefficient k depends on physical parameters such as the size and distance of the transmitting and receiving coils. Therefore, we analyzed the simple configuration shown in Fig. 13 for the purpose of quantitatively understanding the parameter dependence on the k value [26]–[28].

The coupling coefficient k is given by the following equation, where L_1 and L_2 are the coil inductances and M is the mutual inductance.

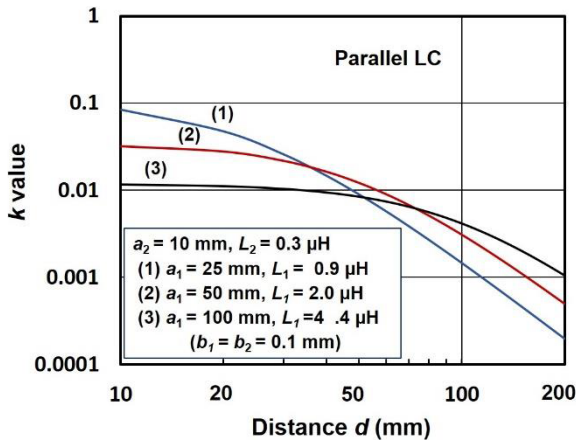


Fig. 14 k value estimation of single ring coil coupling.

$$k = \frac{M}{\sqrt{L_1 \cdot L_2}} \quad (3)$$

In this formula, the inductance L of the single-loop coil is

$$L = a \cdot \mu_0 \cdot \left(\log \frac{8a}{b} - \frac{7}{4} \right) \quad (4)$$

Where parameter a is coil radius, b is the radius of the coil conductor, and μ_0 is the space permeability. Mutual inductance M can be obtained by following Neumann's formula.

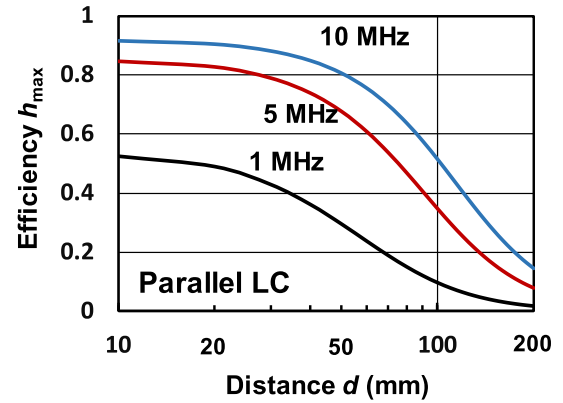
$$M = \frac{\mu_0}{4\pi} \int_0^{2\pi} \int_0^{2\pi} \frac{a_1 \cdot a_2 \cdot \cos(\theta_1 - \theta_2) \cdot d\theta_1 \cdot d\theta_2}{\sqrt{a_1^2 + a_2^2 + d^2 - 2a_1 \cdot a_2 \cdot \cos(\theta_1 - \theta_2)}} \quad (5)$$

where a_1 and a_2 are for the radius of the coils, θ_1 and θ_2 are the angular coordinates, respectively, and d is the distance between two coils.

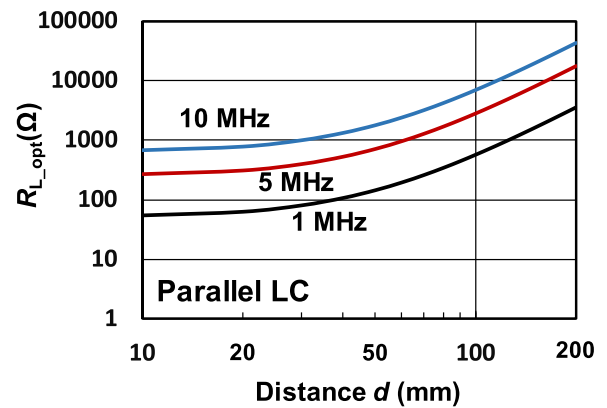
Figure 14 shows the calculation results of the relationship between the distance d between the transmitting and receiving coils and the coupling coefficient k using the equations above. The characteristics of the three wires are obtained when the radius of the receiving coil on the sensor circuit side is fixed to a small size of 10 mm, and the radius of the transmitting coil is set to 25 mm, 50 mm, and 100 mm. From this result, when the size of the transmission coil is increased, the value of k at $d = 10$ mm decreases, but the attenuation rate slows down as d increases. When the size of the transmitting coil is small, k is high at short distances, but it attenuates rapidly as d increases. Considering long-distance power transmission, it is better to set the size of the coil on the transmission side larger.

Figure 15 shows the calculation results of the d dependence of the maximum efficiency η_{\max} and the optimum load $R_{L_{\text{opt}}}$ using the k values of line (2) in Fig. 14, and equations of η_{\max} and $R_{L_{\text{opt}}}$ equations for the parallel LC structure in Table 2.

The three characteristics in Figure 15 are the results of calculations assuming three different resonance frequencies. As the resonant frequency increases, the Q value of



(a) Efficiency



(b) optimum load value

Fig. 15 Distance dependence of efficiency and optimum load value.

the coil increases, resulting in improved efficiency and the optimum load of high resistance. It is preferable to set the resonance frequency to a higher value for power supply to a sensor module that operates with small power and is a high-resistance load.

4.3 Experiment of Wireless Power Transfer

Based on the above basic results, the transmitting and receiving coils were designed and created on printed circuit boards [29], [30], respectively, and wireless power transmission experiments were conducted. Figure 16 shows fabricated PCB coils. The transmitting side has a 100 mm square spiral configuration, and the receiving side used as a sensor terminal has a 20 mm square. The reason for adopting a square shape is to make it possible to utilize the component mounting space as a module. The number of turns N was set appropriately to obtain a large mutual inductance value M . In order to reduce the resistance loss for the high Q operation, the line width of the transmission coil was 2 mm, and the gap between the lines was 0.2 mm. The receiving coil has a wire width of 0.3 mm and secures 6 turns on a small PCB, with a gap of 0.3 mm.

Figure 17 shows the evaluation results of these coils

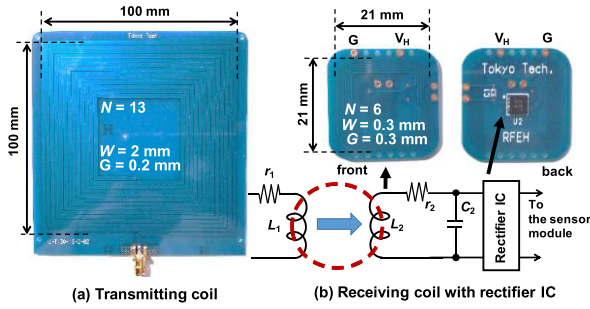


Fig. 16 Transmitting and receiving coils on PCB.

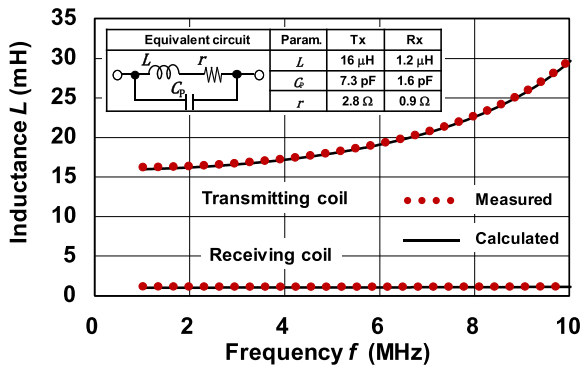


Fig. 17 Inductance of coils on PCB.

and their modeling results. It shows the frequency dependence of the inductance value L up to 10 MHz. The receiving coil has almost no frequency dependence, but the inductance value of the transmitting coil increases as the frequency increases. This is due to the large line-to-line capacitance of the coil C_p , and the effect of improving the Q value can be expected when the frequency is set to be high. The dashed line is the result of the calculation using the equivalent circuit model in the figure that considers the line-to-line capacitance C_p and resistance loss r , and it agrees well with the actual measurement result.

Using these equivalent circuit models, the coupling characteristics between the transmitting and receiving coils were simulated. Figure 18 shows the simulated frequency response of coupling between transmitting and receiving coils. In the equivalent circuit, the tuning capacitances of C_{ts} and C_{tr} were adjusted so that the resonance frequency f_{r1} on the transmitting side and the f_{r2} on the receiving side were 5 MHz. Here, the resistance r_{rec} and the capacitance C_{rec} are parameters that express the rectifier circuit. Since the rectifier circuit behaves non-linearly, a linear model was used for analysis with ease although it is not exact. Considering the capacitance of the assumed rectifier circuit was as large as 500 pF and L_2 value from Fig. 17, the resonance frequency was set to 5 MHz. C_{ts} acts as C_1 in the equivalent circuit of Table 2, and the parasitic capacitance C_{p1} of L_1 acts to increase the inductance value of L_1 . C_2 in Table 2 is the sum of the parasitic capacitance C_{p2} of L_2 , C_{tr} , and C_{rec} .

In the simulation, the input signal is assumed to be a sine wave of 20 V_{p-p}, and the received DC voltage V_r is a

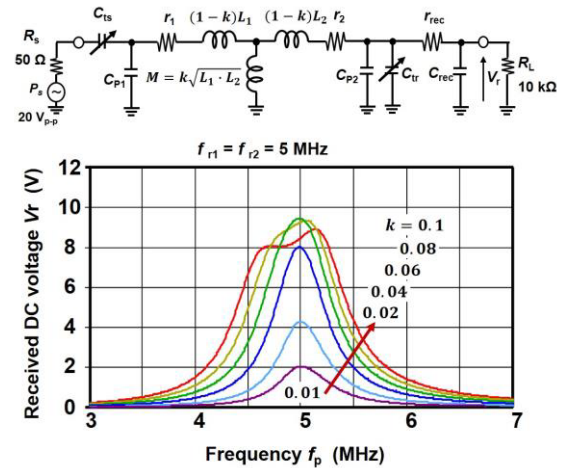


Fig. 18 Simulated frequency response of coupling between transmitting and receiving coils on PCB.

value calculated by assuming the lossless full-wave rectification and smoothing operations. The load R_L was set to 10 k Ω . As a result, if the coupling coefficient k is greater than 0.01, we can expect the V_r greater than the voltage 2 V (current 200 μ A) that is enough for driving the sensor interface IC described in the Sect. 3. The IC can be operated with the voltage more than 1 V.

Also, when the k value is greater than 0.06, two peaks appear in Fig. 18 and the received voltage V_r drops as described in Sect. 4.1.

Wireless power transmission (WPT) experiments were performed to confirm the validity of these simulation results. A 4.2 mm \times 3.7 mm rectifier IC (NMLU1210 [31]) was mounted on the receiving side PCB coil, as shown in the photo in Fig. 16(b), and the output voltage was measured against a 10-k Ω load. As a signal source on the transmitting side, a waveform generator (Agilent 33500B) was used to supply a 20-V_{p-p} amplitude output to the transmitting coil.

Figure 19 shows the evaluation results. The frequency responses were measured with the transmitting coil and the receiving coil facing each other in parallel. A plurality of characteristics emerges when the distance d is changed from 5 mm to 105 mm in 10 mm steps. It can be seen that the received DC voltage monotonically decreases as the distance d increases. Even when the distance d is 105 mm, we obtained a receiving voltage V_r of about 1 V at 5 MHz that can drive the sensor interface IC. When the frequency f_p is shifted to 5.1 MHz, the voltage V_r becomes 2 V with peak splitting.

However, this result does not match the simulation result of Fig. 18. In Fig. 18, the voltage V_r monotonously decreases in the region where the k value is lower than 0.06, but two peaks do not appear and do not agree with the evaluation results.

In the experiment, it was not easy to tune the resonance frequency by controlling the capacitance value, especially for the transmitting side because the inductance value was large. Therefore, considering the possibility that the

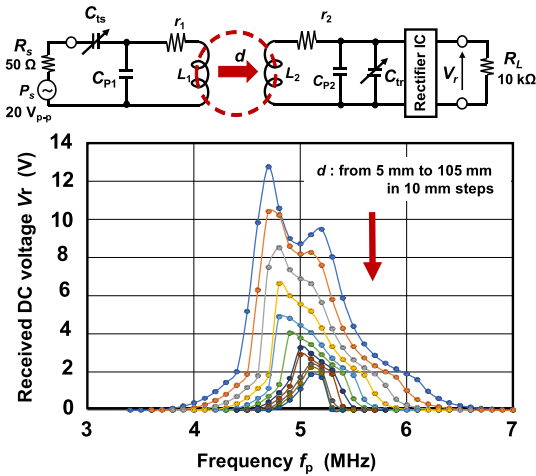


Fig. 19 Measured frequency response of coupling between transmitting and receiving coils on PCB.

frequencies of the transmitting side and the receiving side are different, the frequency response was re-simulated with that the resonance frequency f_{r1} is 4.75 MHz and the f_{r2} is 5.25 MHz by the tuning capacitances of C_{ts} and C_{tr} precisely. The results are shown in Fig. 20. As in the experimental results, two peaks appear, and it can be seen that the voltage V_r decreases monotonically as the k value decreases.

Compared to the simulation results in Fig. 18, the voltage V_r has dropped from 4.2 V to 1 V when the k value is 0.02. Also, the voltage V_r increases monotonously even when the k value is greater than 0.06. It is considered that this is because the resonance effect decreases due to the difference in resonance frequency between the transmitting and the receiving sides.

By matching the resonance frequencies with higher accuracy, it is expected that a higher voltage V_r can be obtained in a region where the k value is low. However, since the target is satisfied when use the characteristics of Fig. 19 as the power transmission characteristics in our application, it is tolerated.

Conversely, it is possible to widen the operating band by intentionally setting a difference between the resonant frequencies, but this is a trade-off with the resonance effect.

Considering that the experimental result of Fig. 19 agrees with Fig. 20 roughly, the distance dependence of the k value of the experimental system was obtained and plotted on the graph of the basic characteristic analysis results of Fig. 14. The results are shown in Fig. 21. Although it is not accurate to compare with the theoretical analysis results of single circular coils, the distance dependence of the k value is showing the same trend as the distance dependence of the single coil (3). The change in k value ranges from 0.095 to 0.02 for a distance of up to 100 mm, which is thought that about 10 times larger due to the multi-turn configuration.

In addition, since the results in Fig. 19 were obtained with the transmit and receive coils centered, the effect of horizontal misalignment shown in Fig. 22 was also evaluated. As the transmitting coil is 100 mm square and is

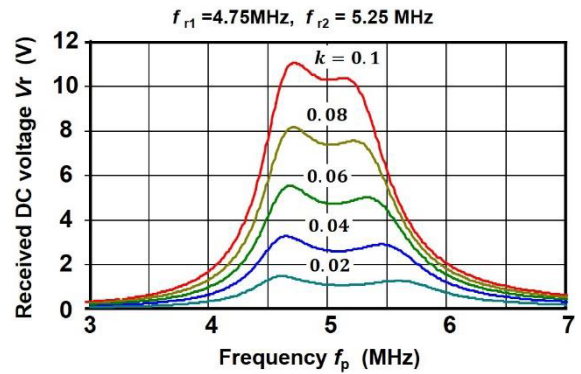


Fig. 20 Simulated frequency response with the resonance frequency difference between transmitting and receiving coils on PCB.

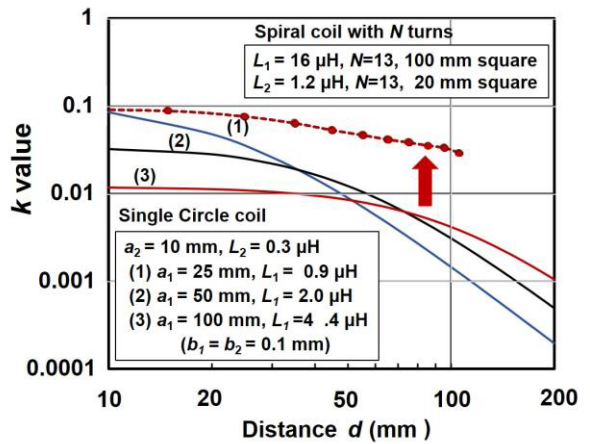


Fig. 21 Relation between k value and distance d .

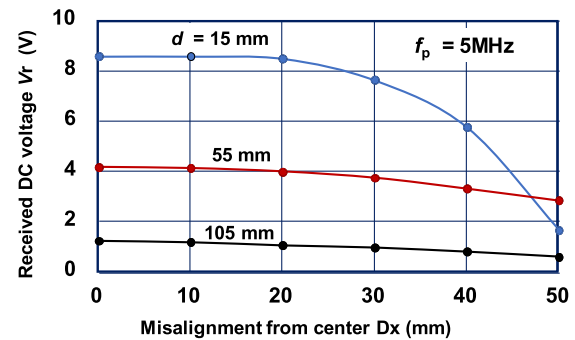


Fig. 22 Effect of horizontal misalignment of transmitting coil and sensing module.

symmetrical, the effect of horizontal misalignment Δx up to 50 mm from the center to the edge was evaluated. These are the characteristics when the frequency f_p is 5 MHz. As the size of the receiving coil module is 20 mm square, which is small compared to the transmitting coil size, it can be seen that there is almost no effect of misalignment up to about 20 mm. From this result, it can be said that power transmission is possible even with rough alignment.

5. Backscatter Sensing with Electromagnetic Coupling

Figure 23 shows the result of obtaining the impedance at the signal source terminal P_1 on the transmission side and calculating the reflection coefficient Γ_{BS} . The Γ_{BS} is low in the 4 to 6 MHz frequency range where wireless power transmission is available. The black line shows the characteristics when the coil on the receiving side is short-circuited with a switch, and it is evident that the amount of reflection is greater than when the switch is open. When switching between the short and open states, the wireless power transmission frequency f_p is modulated by the switching frequency f_s and reflected back to the transmission side.

Figure 24 shows the result of simulating the reflected signal voltage waveform and its frequency spectrum when the coupling coefficient k is assumed to be 0.06, f_p is 5 MHz,

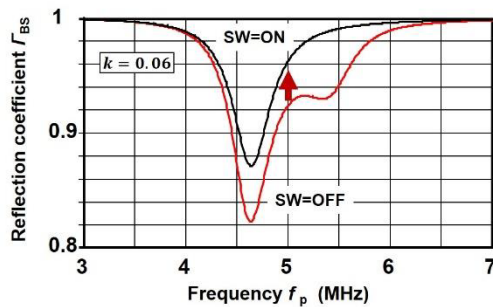
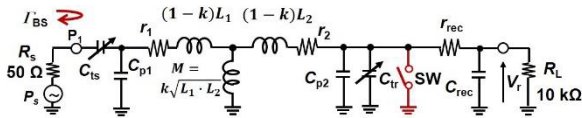
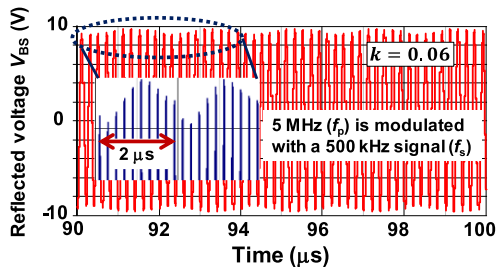
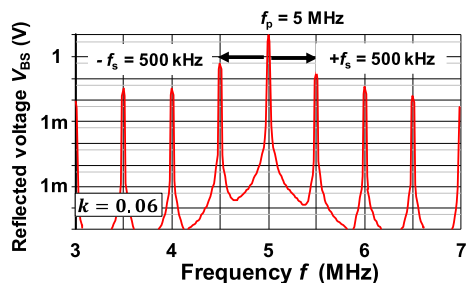


Fig. 23 Reflection coefficient (simulated).



(a) Wave form of reflected signal modulated



(b) Frequency spectrum of reflected signal modulated

Fig. 24 Backscatter signal sensing (simulated).

and the switching frequency f_s of the receiving side coil was set to 500 kHz. As shown in Fig. 9, the oscillation frequency output of the sensor interface circuit ranges from 40 kHz to 1000 kHz, so 500 kHz was selected as a representative value in this simulation. Although the modulation is as low as 4%, the switching frequency f_s of the receiving side coil can be captured as a backscatter signal from the frequency spectrum.

By using the output of the circuit that transforms the sensor information into the frequency domain shown in Fig. 4 as f_s , sensor state changes can be captured wirelessly as changes in the frequency of the backscatter signal. The switch for realizing this modulation is built into the sensor interface IC. As illustrated in Fig. 6, the switch M_{BS} is composed of MOSFET and switched by the output of the oscillation circuit. The gate length of the MOSFET is $0.7 \mu m$, and the gate width is set to $196 \mu m$ ($7 \text{ mm} \times 28$ fingers) so as to ensure a small on resistance during on/off operation. The MOSFET does not consume power because it only changes the output resistance value for the reflecting operation.

The feasibility of wireless sensing by backscatter will be shown in the evaluation results of the prototype battery-less wireless sensing module in the next section.

6. Battery-Less Wireless Sensing

By combining the three circuit technologies discussed in Sessions 3 to 5, an experiment was conducted to wirelessly monitor the temperature of the blind space without batteries.

The sensor interface board shown in Fig. 7(b) and the receiving coil board shown in Fig. 16(b) are stacked as shown in Fig. 25 to form the proposed wireless sensing module that operates without the battery. The sensor interface board is equipped with a $100 \text{ k}\Omega$ NTC chip thermistor [32] as an environmental temperature detection sensor. The parameter values were set so that the frequency varied from 200 kHz to 700 kHz with respect to temperature changes from 0°C to 60°C . The thermistor has a B-constant of 4250 K , and the resistance changes from $400 \text{ k}\Omega$ to $22 \text{ k}\Omega$.

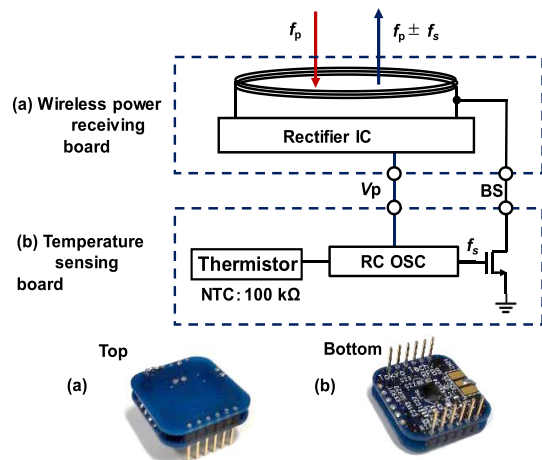


Fig. 25 Battery-less wireless temperature sensing module.

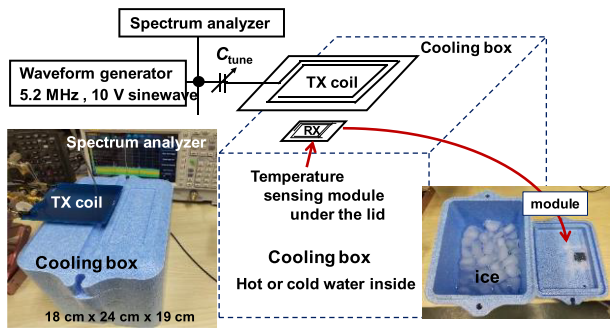


Fig. 26 Experimental system.

A chip capacitance of 22 pF was selected as C_s in Fig. 6 based on the analysis results of Fig. 9. And if the thermistor is connected directly as R_s , the oscillation will stop if the resistance drops below 20 k Ω . To prevent this, a 10 k Ω chip resistor was connected in series with the thermistor as insurance. When the temperature is 25°C, the oscillation frequency is designed to be 300 kHz based on Eq. (1). At 0°C and 60°C, they are 185 kHz and 660 kHz respectively.

In order to confirm the wireless temperature sensing operation without a battery, we attached the module to the back of the lid of the cool box (18 cm \times 24 cm \times 19 cm) as shown in Fig. 26, and tried to measure the temperature inside the box. Temperature changes within the box are detected as frequency changes in the oscillator circuit. In order to get the relationship between the frequency and the temperature inside the box, the experiment was conducted while monitoring the temperature inside the box with a thermocouple device. The temperature inside the box was controlled using cold and hot water. A Waveform generator (Agilent 33500B) supplied power to the TX coil antenna and the backscatter signal was monitored with a spectrum analyzer (RIGOL RSA3030-TG). The distance between the transmitting antenna coil TX and the receiving antenna coil RX inside the box is about 50 mm and the maximum could reach 100 mm.

Figure 27 shows the measured frequency spectrums. The upper spectrum is characteristic when the temperature inside the box is 10°C and the lower one is 29°C. It detected 215 kHz at 10°C and 332 kHz at 29°C, and successfully wirelessly sensed the temperature inside the box without a battery.

Figure 28 shows the results of evaluating the relationship between the temperature inside the box and the sensing frequency. From this relationship, by monitoring the frequency, the temperature inside the box in the blind environment can be detected without opening the lid.

The dashed line is the result calculated based on Eq. (1), which agrees well with the actual measurement result. Sensitivity to temperature can be arbitrarily adjusted by changing the variation range of the R_s value and the C_s value.

Table 3 shows the specifications of the prototype module. The target properties shown in Table 1 were realized.

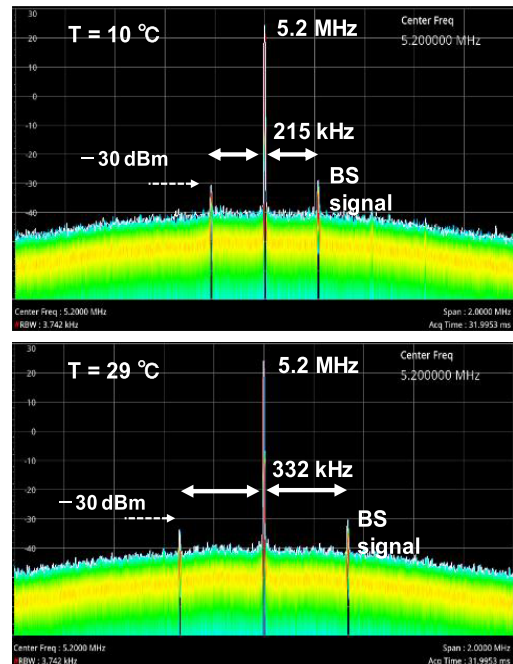


Fig. 27 Measured frequency spectrum of backscatter signal from sensing module.

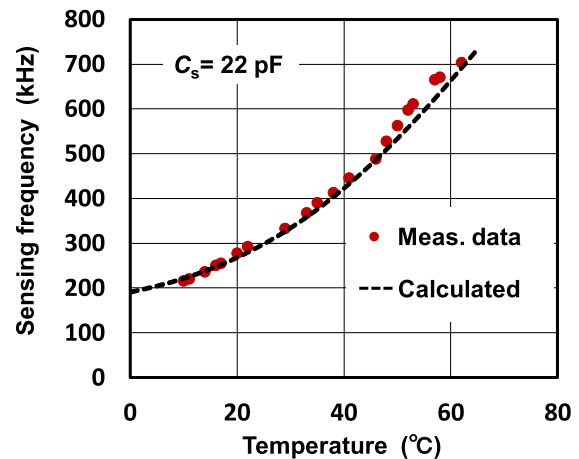


Fig. 28 Measured relationship between temperature and sensing frequency in cooling box.

In this experiment, a temperature sensor was mounted, but it is also possible to mount capacitive and resistance-type sensors such as humidity, strain, pressure, tilt, and so on. Additionally, further miniaturization is possible by reducing test terminals.

7. Conclusion

We have designed and built a battery-less wireless sensing system that enables the monitoring of closed spaces and obtained the following results.

- (1) Sensor interface circuit technique: It is analytically clarified that an RC relaxation oscillator circuit, which can be

Table 3 Summary of prototype sensing system.

Item	Functions/Values
Target Application	Sensing in invisible areas (delivery boxes, structural buildings, and living organisms)
Module Operation	Wireless & Battery-less
Communication distance	up to 100 mm
Sensing circuit	RC oscillator
Sensing frequency	100 kHz to 1MHz (FM modulated)
Connectable sensors	Capacitor and resistance type
Wireless sensing	Signal backscattering
Power consumption	Less than 1mW
Wireless power supply	Electromagnetic coupling
Power supply frequency	5.2 MHz
Module size	2.5 cm x 2.5 cm x 0.8 cm (5 cc)

directly connected to a sensor and can convert its information to the frequency domain, is suitable for low-power operation. Furthermore, in order to obtain a more compact and highly reliable operation, we integrated the circuit using 0.7- μm CMOS technology and succeeded in realizing a 758 kHz oscillation operation with a power supply voltage of 1V and a current consumption of 24.5 μA .

(2) Wireless power transfer technique with magnetic resonant coupling: The power transfer characteristics to a small coil were clarified analytically, and a design guideline was obtained. Based on this, a transmitter coil, and a receiver coil were prototyped and evaluated. As a result, we achieved power transmission characteristics that almost match the analysis results.

(3) Backscatter sensing technique: It was confirmed by simulations and experiments that sensor information can be backscattered to the transmitting side by switching the receiving-side resonance circuit with the oscillation circuit output of the sensor interface.

(4) Blind space monitoring: By combining the three circuit technologies, an experiment was conducted to wirelessly monitor the temperature of the blind space without batteries. As a result, we succeeded in monitoring the temperature inside the cool box without opening the lid as designed.

The battery-less, wireless sensing technology based on the fusion circuit technology described in this paper will greatly contribute to the collection of various information in the IoT era.

Acknowledgments

We are grateful to New Japan Radio Co., Ltd. (now Nisshinbo Microdevices Inc.) for their cooperation in the design and manufacture of 0.7- μm CMOS integrated circuits.

References

- [1] T. Lynn, P.T. Endo, A.M.N.C. Ribeiro, G.B.N. Barbosa, and P. Rosat, "The Internet of Things: Definitions, key concepts, and reference architecture," *The Cloud-to-Thing Continuum*. Palgrave Studies in Digital Business & Enabling Technologies. Palgrave Macmillan, Cham., July 2020, https://doi.org/10.1007/978-3-030-41110-7_1
- [2] Q. Du, H. Song, and X. Zhu, "Social-feature enabled communications among devices toward the smart IoT community," *IEEE Commun. Mag.*, vol.57, no.1, pp.130–137, Jan. 2019, DOI: 10.1109/MCOM.2018.1700563.
- [3] I. Popova, E. Abdullina, I. Danilov, A. Marusin, A. Marusin, I. Ruchkina, and A. Shemyakin, "Application of the RFID technology in logistics," *Transportation Research Procedia*, vol.57, pp.452–462, 2021, DOI: 10.1016/j.trpro.2021.09.072.
- [4] B. Yan and D. Lee, "Application of RFID in cold chain temperature monitoring system," *Digest of 2009 ISECS International Colloquium on Computing, Communication, Control, and Management*, pp.258–261, 2009.
- [5] H. Kim, J. Ahn, J. Rhee, and S. Ahn, "Application of wireless power transfer technology to implantable medical devices," *Digest of 2022 IEEE MTT-S International Microwave Biomedical Conference (IM-BioC)*, DOI: 10.1109/IMBioC52515.2022.9790118.
- [6] D. Jayawardana, S. Kharkovsky, and R. Liyanapathirana, "Measurement system with a RFID tag antenna mounted on structural members for infrastructure health monitoring," *Proc. 2015 IEEE international Instrumentation and Measurement Technology Conference (I2MTC)*, 2015, DOI: 10.1109/I2MTC.2015.7151231.
- [7] B.A. Mouris, W. Elshennawy, P. Petridis, Y. Ding, and S.N. Daskalakis, "Rectenna for Bluetooth low energy applications," *Proc. 2019 IEEE Wireless Power Transfer Conference (WPTC)*, June 2019, DOI: 10.1109/WPTC45513.2019.9055609.
- [8] M.M. Mansour, O. Takiguchi, T. Inoi, and H. Kanaya, "Experimental investigation of wireless energy harvesting with a Bluetooth low energy sensing unit," *Proc. 2018 International Conference on Electronics Packaging and iMAPS All Asia Conference (ICEP-IAAC)*, TD4-4, 2018, DOI: 10.23919/ICEP.2018.8374700.
- [9] U. Raza, P. Kulkarni, and M. Sooriyabandara, "Low power wide area networks: An overview," *IEEE Commun. Surveys Tuts.*, vol.19, no.2, pp.855–873, 2017, DOI: 10.1109/COMST.2017.2652320.
- [10] G.H. Derevianckine, A. Guillon, O. Iova, B. Ning, and F. Valois, "Opportunities and challenges of LoRa 2.4 GHz," *IEEE Commun. Mag.*, vol.61, no.10, pp.164–170, Feb. 2023, DOI: 10.1109/MCOM.010.2200566.
- [11] B. Razavi, *RF Microelectronics*, 2nd ed., Prentice Hall, 2011.
- [12] T.H. Lee, *The Design of CMOS Radio-Frequency Integrated Circuits*, Cambridge University Press, 2004.
- [13] B. Xia, N. Qi, L. Liu, and N. Wu, "A low-power 2.4 GHz Zig-Bee transceiver with inductor-less RF front-end for IoT applications," *2017 IEEE 60th International Midwest Symposium on Circuits and Systems (MWSCAS)*, pp.1332–1335, 2017, DOI: 10.1109/MWSCAS.2017.8053177.
- [14] K. Shibata, H. Matsui, H. Asano, Y. Kusaka, K. Ueda, N. Matsuno, and H. Sato, "A 22 nm 0.84 mm² BLE transceiver with self IQ-phase correction achieving 39 dB image rejection and on-chip antenna impedance tuning," *Digest of 2022 IEEE International Solid - State Circuits Conference (ISSCC)*, Session 24, 24.4, pp.398–399, 2022, DOI: 10.1109/ISSCC42614.2022.9731558.
- [15] E. Lu, W.-K. Li, Z. Deng, E. Rostami, P.-A. Wu, K.-M. Chang, Y.-C. Chuang, C.-M. Lai, Y.-C. Chen, T.-H. Peng, T.-C. Tsai, H.-H. Liu, C.-C. Chiu, B. Huang, Y.-C. Wang, J.-H.C. Zhan, and O. Shanaa, "A 4 × 4 dual-band dual-concurrent WiFi 802.11ax transceiver with integrated LNA, PA and T/R switch achieving +20 dBm 1024-QAM MCS11 pout and −43 dB EVM floor in 55 nm CMOS," *Digest of 2020 IEEE International Solid-State Circuits*

- Conference (ISSCC), Section 10, 10.4, pp.178–179, 2020, DOI: 10.1109/ISSCC19947.2020.9063127.
- [16] H. Shan, J. Peterson, III, S. Hathorn, and S. Mohammadi, “The RFID connection: RFID technology for sensing and the Internet of Things,” *IEEE Microw. Mag.*, vol.19, no.7, pp.63–79, 2018, DOI: 10.1109/MMM.2018.2863439.
- [17] R. Correia, D. Belo, F. Pereira, M. Jordão, and N.B. Carvalho, “Backscatter modulation for wearable devices: A backscatter modulator, consisting of an antenna and a 1-MHz binary backscatter modulator operating at a carrier frequency of 915 MHz,” *IEEE Microw. Mag.*, vol.20, no.1, pp.78–84, 2019, DOI: 10.1109/MMM.2018.2875632.
- [18] J. Ko and M. Lee, “A 1.8 V 18.13 MHz inverter-based on-chip RC oscillator with flicker noise suppression using logic transition voltage feedback,” *Electronics*, vol.8, no.11, p.1353, 2019, DOI:10.3390/electronics8111353
- [19] Foundry service, “0.7 um LV CMOS With HV CMOS for Analog IC,” SG-6, New Japan Radio Co., Ltd. (Nisshinbo Microdevices Inc.).
- [20] D. Griffith, P.T. Røine, J. Murdock, and R. Smith, “A 190 nW 33 kHz RC oscillator with $\pm 0.21\%$ temperature stability and 4 ppm long-term stability,” *Digest of 2014 IEEE International Solid-State Circuits Conference (ISSCC), Session 17, 17.8*, pp.300–301, 2014.
- [21] H. Hirayama, “Basic lecture of magnetic coupling wireless power transfer,” 2015 Microwave Workshop and Exhibition (MWE), Workshop Digest, TH1A-1, 2015 (in Japanese).
- [22] N. Shinohara and K. Komurasaki, *Wireless Power Supply Technology*, Kagaku-Gizyutsu Syupan, 2013 (in Japanese).
- [23] J. Sallán, J.L. Villa, A. Llombart, and J.F. Sanz, “Optimal design of ICPT systems applied to electric vehicle battery charge,” *IEEE Trans. Ind. Electron.*, vol.56, no.6, pp.2140–2149, 2009, DOI: 10.1109/TIE.2009.2015359.
- [24] T. Hiramatsu, X. Huang, M. Kato, T. Imura, and Y. Hori, “Independent control of maximum transmission efficiency by the transmitter side and power by the receiver side for wireless power transfer,” *IEEJ Trans. IA*, vol.135, no.8, pp.847–854, 2015, DOI: 10.1541/ieejias.135.847.
- [25] C.M. Zierhofer and E.S. Hochmair, “Geometric approach for coupling enhancement of magnetically coupled coils,” *IEEE Trans. Biomed. Eng.*, vol.43, no.7, pp.708–714, 1996, DOI: 10.1109/10.503178.
- [26] T. Imura, H. Okabe, T. Uchida, and Y. Hori, “Study of magnetic and electric coupling for contactless power transfer using equivalent circuits,” *IEEJ Trans. IA*, vol.130, no.1, pp.84–92, 2010.
- [27] K. Goto and S. Yamazaki, *Detailed Explanation Electromagnetism Exercise*, 47th ed., Chapter 8, Kyoritsu Syupan, 1978 (in Japanese).
- [28] S. Konno, T. Yamamoto, and K. Koshiji, “Investigation of coupling coefficient characteristics between printed spiral coil and simple loop coil,” 23rd Microelectronics Symposium (MES2013), 1C2-2, pp.101–104, 2013 (in Japanese).
- [29] A.B. Islam, S.K. Islam, and F.S. Tulip, “Design and optimization of printed circuit board inductors for wireless power transfer system,” *Circuit and Systems*, vol.4, no.2, pp.237–244, 2013, DOI: 10.4236/cs.2013.42032.
- [30] B. Noroozi and B.I. Morshed, “Formal method for PSC design optimization of 13.56 MHz resistive wireless analog passive sensors (rWAPS),” 2016 IEEE Topical Conference on Biomedical Wireless Technologies, Networks, and Sensing Systems (BioWireless), pp.8–11, 2016, DOI: 10.1109/BIOWIRELESS.2016.7445547.
- [31] Data Sheet, “NMLU1210: Full Bridge Rectifier,” ON Semiconductor, Rev.1, Aug. 2013.
- [32] Data Sheet, “NCP18WF104F12RB,” Murata Manufacturing Co., LTD.



Zixuan Li received the B.E. degree in electronic information engineering from the Beihang University, Beijing, China, in 2017, and the M.E. degree in electrical and electronic engineering from the Tokyo Institute of Technology, Yokohama, Japan in 2020. She is currently pursuing the Ph.D. degree in electrical and electronic engineering with the Tokyo Institute of Technology. Her current research interests include wireless sensors and sensing technology, and low-power Internet-of-Things devices.



Sangyeop Lee received the B.E. degree in electrical and electronic engineering from the Tokyo Institute of Technology, Tokyo, Japan, in 2009, and the M.E. and Ph.D. degrees in electronics and applied physics from the Tokyo Institute of Technology, Yokohama, Japan, in 2010 and 2013, respectively. After working for a Korean research institute, Agency for Defense Development (ADD), Daejeon, South Korea, he joined Hiroshima University, Higashihiroshima, Japan, as a Researcher and an Assistant Professor, from 2017 to 2020. In 2020, he joined the Tokyo Institute of Technology, where he is currently an Assistant Professor. His current research interests include design of millimeter-wave/terahertz CMOS circuits and IoT sensors.



Noboru Ishihara received the B.S. degree in electrical engineering from Gunma University, Gunma, in 1981 and the Dr. Eng. Degree from Tokyo Institute of Technology, Tokyo, Japan, in 1997. During 1981–2004, he stayed the Electrical Communication Laboratory, NTT, Japan, where he has been engaged in research and development of analog IC’s for communication use. From 2004 to 2007, he was a Visiting Professor of Gunma University, Japan. In 2008, He joined Tokyo Institute of Technology. His research interest is in the area of analog IC’s and modules for wireless and optical communications. Dr. Ishihara is a member of the IEEE Microwave Theory and Technique Society and Solid-State Circuit Society, and the Institute of Electronics, Information and Communication Engineers (IEICE).



Hiroyuki Ito received the B.E. degree from the Department of Electronics and Mechanical Engineering, Chiba University, Chiba, Japan, in 2002, and the M.E. and Ph.D. degrees from the Department of Advanced Applied Electronics, Tokyo Institute of Technology, Yokohama, Japan, in 2004 and 2006, respectively. From 2004 to 2007, he was a Research Fellow of the Japan Society for the Promotion of Science. He was a temporary Visiting Researcher and a Visiting Professor with the Communications Tech-

nology Laboratory, Intel Corporation, Hillsboro, OR, USA, in 2006 and 2007, respectively. He was an Assistant Professor at the Precision and Intelligence Laboratory, Tokyo Institute of Technology, from 2007 to 2013, where he was an Associate Professor from 2013 to 2015. From 2008 to 2010, he was with Fujitsu Laboratories Ltd., Yokohama, where he developed an RF CMOS transceiver and digital calibration techniques for mobile WiMAX applications. Since 2016, he has been an Associate Professor with the Institute of Innovative Research, Tokyo Institute of Technology. He has been the Co-Funder/CEO of Evrim Company Ltd., Yokohama, since 2020. His research interests include ultralow-power RF circuits, a high-sensitivity MEMS accelerometer, a low-noise and crystal-less RF synthesizer, a cow management system exploiting the Internet of Things (IoT), and deep/machine learning. Dr. Ito is a member of the IEEE Solid-State Circuits Society, the Institute of Electronics, Information and Communication Engineers (IEICE), the Japan Society of Applied Physics (JSAP), and the Japanese Society of Agricultural Machinery and Food Engineers. He is also an International Technical Program Committee Member of the International Solid-State Circuits Conference. He was a recipient of the European Solid-State Circuits Conference (ESSCIRC) 2008 Best Paper Award.